Eur. Phys. J. Plus (2018) **133**: 195
DOI 10.1140/epjp/i2018-12002-6

THE EUROPEAN PHYSICAL JOURNAL PLUS

Regular Article

Impact of Cattaneo-Christov heat flux on electroosmotic transport of third-order fluids in a magnetic environment

J.C. Misra[1], B. Mallick[1], A. Sinha[2], and A. Roy Chowdhury[1,a]

[1] Centre for Healthcare Science and Technology, Indian Institute of Engineering Science and Technology, Shibpur, Howrah - 711103, India
[2] Department of Mathematics, Yogoda Satsanga Palpara Mahavidyalaya, Purba Medinipur - 721457, India

Received: 14 January 2018 / Revised: 4 April 2018
Published online: 23 May 2018

Abstract. In the case of steady flow of a fluid under the combined influence of external electric and magnetic fields, the fluid moves forward by forming an axial momentum boundary layer. With this end in view a study has been performed here to investigate the problem of entropy generation during electroosmotically modulated flow of a third-order electrically conducting fluid flowing on a microchannel bounded by silicon-made parallel plates under the influence of a magnetic field, by paying due consideration to the steric effect. The associated mechanism of heat transfer has also been duly taken care of, by considering Cattaneo-Christov heat flux. A suitable finite difference scheme has been developed for the numerical procedure. A detailed study of the velocity and temperature distributions has been made by considering their variations with respect to different physical parameters involved in the problem. The results of numerical computation have been displayed graphically. The computational work has been carried out by considering blood as the working fluid, with the motivation of exploring some interesting phenomena in the context of hemodynamical flow in micro-vessels. Among other variables, parametric variations of the important physical variables, *viz.* i) skin friction and ii) Nusselt number have been investigated. The study confirms that the random motion of the fluid particles can be controlled by a suitable adjustment of the intensity of an externally applied magnetic field in the transverse direction. It is further revealed that the Nusselt number diminishes, as the Prandtl number gradually increases; however, a steady increase in the Nusselt number occurs with increase in thermal relaxation. Entropy generation is also found to be enhanced with increase in Joule heating. The results of the present study have also been validated in a proper manner.

1 Introduction

Electro-kinetic phenomena constitute a class of some dissimilar types of effects, which are observed in a variety of situations, for example, when fluid flows through porous media and in the case of movement of a fluid that contains solid or liquid particles, or gaseous bubbles of micrometre (1×10^{-6} m) or nanometre (1×10^{-9} m) size. Electrophoresis and electroosmosis are two of the several examples of electrokinetic phenomena (cf. Lyklema [1]). Electro-osmosis (electro-osmotic flow) refers to the motion of a liquid in a porous medium subject to the action of an externally applied electric field, while the motion of particles under the action of an external electric field is called electrophoresis. The Coulomb force induced by an electric field in a solution is supposed to be the cause of electro-osmotic flow (EOF). An electrical double layer (EDL), also simply called a double layer (DL) is associated with the phenomenon of electroosmosis and also with other electro-kinetic phenomena. Electrical double layer refers to two parallel layers of charge that are formed in the vicinity of the surface of an object when it is emerged in a liquid. In fact, the formation of electrical double layers plays a fundamental role in electroosmotic flow of liquids. Another scientific term related to electroosmotic transport is the zeta potential, which refers to the electric potential of interfacial double layer (DL). The stability of colloidal dispersion is known to depend on zeta potential to a great extent. In the case of molecules and small particles, high zeta potential offers better stability.

[a] e-mail: misrajc@gmail.com

Several studies on electroosmotic flows have been carried out by different researchers. Some of them also dwelt on the applications of EOF studies in micro-reactors [2–4], heat transfer in electronic devices and biomedical sensors [5], drug delivery [6,7], etc. Arifin *et al.* [8] studied the electrohydrodynamic flow of blood and discussed the separation procedure of red blood cells from blood plasma in a miniaturized device. A study of rotational electro-hydrodynamic microflows of a viscoelastic fluid considering electrical double layer effect was reported by Abhimanyu *et al.* [9]. A problem relevant to the influence of Hall current and rotation of micro-particles on the boundary layer flow of an electrically conducting fluid, *e.g.*, blood was recently discussed by Chandra and Misra [10]. The estimate of flow in bio-fluidic devices was reported by Misra *et al.* [11], on the basis of their study on the flow of a micropolar fluid in a micro-channel under the influence of an alternating electric field. Another study on electro-osmotic flow of a different type of non-Newonian fluid in a circular microtube was conducted by Tan and Liu [12]. Electroosmotic oscillatory flow of blood in microfluidic devices was discussed by Misra *et al.* [13]. In a separate communication, electro-osmotically actuated flow of blood on a porous micro-channel was discussed by Misra and Chandra [14], for a situation, when the micro-channel is under the influence of an externally applied AC electric field with different frequencies. Two other separate studies on electroosmotic flows in viscoelastic/second-grade were conducted by Misra *et al.* [15,16].

Similarly, several researchers have studied magneto-hydrodynamic flows of physiological fluids, with particular reference to blood flow in arteries/capillaries of different dimensions. Magnetohydrodynamics of blood flow under the action of a strong magnetic environment was studied by Keltner *et al.* [17]. Tzirtzilakis [18] studied the effect of an externally applied magnetic field, considering blood as a Newtonian fluid. A theoretical analysis of the magnetic field interaction with aortic blood flow under the influence of a static magnetic field, was presented by Kinouchi [19]. A numerical simulation of MHD mixed convection of a viscous dissipating fluid on a permeable vertical flat plate was presented by Aydin and Kaya [20]. A brief account of many of these are available in our earlier publications (Misra *et al.* [21–33]). However, none of the aforesaid studies takes care of situations, where the system is subject to the combined influence of externally applied electric and magnetic fields. On the basis of the experimental observation that blood behaves as a non-Newtonian fluid, several researchers formulated different mathematical models by considering blood as a second-order viscoelastic fluid (cf. [34–37]). However, the constitutive equations used in these models are inadequate to depict the shear thickening/shear thinning properties, although they can take care of the normal stress differences. This observation emphasizes the necessity of considering higher order models for complex fluids possessing shear thinning/shear thickening properties.

In view of the observations made above, we have considered a third-order fluid model in the present study of electroosmotic flow and heat transfer under the combined influence of electric and magnetic fields, applied externally, since the study is motivated towards exploring some interesting information on the flow and heat transfer of blood, which is known to be a complex fluid. Here, the heat transfer has been studied by considering the Cattaneo-Christov heat flux model. It is worthwhile to mention here that most of the heat transfer problems studied by various researchers are based on Fourier's law of heat conduction. Although this law bears the potential to explain the heat transfer phenomena in a variety of situations, the main drawback of using this law is that it gives a parabolic energy equation for the temperature field, leading to the so-called "paradox of heat conduction". This has been discussed by Hayat *et al.* [38] Mustafa [39] and Han *et al.* [40]. This difficulty can be removed by adding in the heat conduction equation a term that involves relaxation time, since Cattaneo's heat conduction equation gives rise to hyperbolic energy equation. Christov [38] made a further generalization of Cattaneo's law, by making the equation frame-invariant. The generalized heat conduction equation is referred to in the literatures as the Cattaneo-Christov heat flux model. The uniqueness of the solution of Cattaneo-Christov heat conduction was established by Ciarletta and Straughan [41]. Sarkar and Kundu [42] studied the effect of Cattaneo-Christov heat flux on the transfer of heat and mass during Maxwell nanofluid flow over a sheet. They performed a numerical simulation and showed that the rate of heat transfer is enhanced in the case of Cattaneo-Christov model, when compared to the case of classical Fouriers model. By using a finite difference scheme, Soomro *et al.* [43] studied the entropy generation in MHD water-based carbon nanotubes and observed that entropy generation reduces as the magnitude of externally applied magnetic field increases. The combined effect of Joule heating, Brownian movement and thermophoresis on MHD Sakiadis flow was studied numerically by Sulochana *et al.* [44]. Afridi *et al.* [45] obtained the exact solution of a problem concerning entropy generation during hydromagnetic boundary flow under the action of frictional and Joule heating. They reported that in comparison to heat transfer, viscous and Joule dissipation generate more entropy.

2 Mathematical modelling

2.1 Description of the model

Let us consider the electro-kinetic transport of a third order fluid on a uniform micro-channel of height $2H$ bounded by two parallel plates, as shown in fig. 1. We take (ξ^*, η^*) as the rectangular cartesian coordinates of a representative point. The walls of the micro-channel are supposed to have uniform surface charge. The zeta potential (ζ) is developed

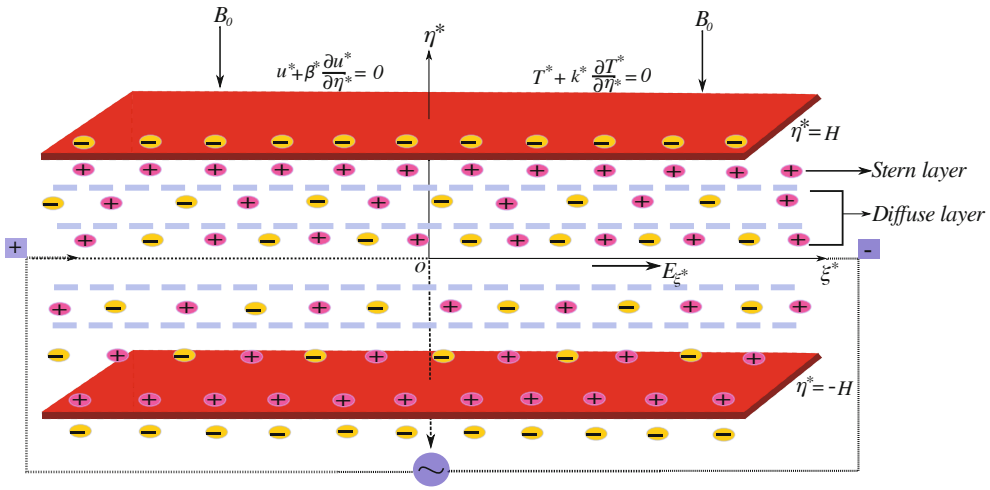

Fig. 1. Physical sketch of the problem.

at the stern layer of the EDL. Formulation of the model has been made based upon the following assumptions:

- The fluid is non-Newtonian, incompressible and electrically conducting.
- The flow is fully developed both hydro-dynamically and thermally.
- The electric field is applied along the axis of the channel.
- Zeta potential is high throughout the medium and it maintains a constant value at the walls of the micro-channel.
- A uniform magnetic field of strength B_0 is applied in the vertical direction.
- Heat transfer is analysed by considering Cattaneo-Christov heat flux.
- Combined effects of Joule heating, magnetic field and viscous dissipation on heat transfer are taken into account.

2.2 Governing equations

The flow field in a uniform rectangular micro-channel of an electrically conducting third order fluid in the presence of a uniform magnetic field B_0 is governed by the continuity equation and the Cauchy momentum equation:

$$\boldsymbol{\nabla}\cdot\boldsymbol{u}^*=0, \tag{1}$$

$$\rho\,\boldsymbol{u}^*\cdot\boldsymbol{\nabla}\boldsymbol{u}^*=\boldsymbol{\nabla}\cdot\boldsymbol{\tau}^*+\boldsymbol{f}_B^*, \tag{2}$$

where ρ denotes the fluid density, $\boldsymbol{u}^*=(u^*,v^*)$ is the velocity vector, $\boldsymbol{\tau}^*$ the stress tensor and $\boldsymbol{f}_B^*$ is the net electromagnetic body force (cf. [46]) given by

$$\boldsymbol{f}_B^*=\rho_e\boldsymbol{E}+(\boldsymbol{J}\times\boldsymbol{B}), \tag{3}$$

in which ρ_e is the total charge density, $\boldsymbol{E}=E_{\xi^*}\boldsymbol{e}_{\xi^*}$ is the applied electric field along the ξ^*-direction, which obeys the Poission-Boltzmann equation and $\boldsymbol{e}_{\xi^*}$ is a unit vector in the ξ^*-direction. $\boldsymbol{J}=\sigma(\boldsymbol{u}^*\times\boldsymbol{B})$ is the electric current density, which follows from Ohm's law [46] with σ as the electrical conductivity. $\boldsymbol{B}=B_0\boldsymbol{e}_{\eta^*}$ is the magnetic field where $\boldsymbol{e}_{\eta^*}$ is a unit vector along the η^*-direction. Considering incompressibility of the fluid, the Cauchy stress tensor $(\boldsymbol{\tau}^*)$ for the fluid under consideration

$$\tau^*=\mu\boldsymbol{A}_1+\alpha_1\boldsymbol{A}_2+\alpha_2\boldsymbol{A}_1^2+\beta_1\boldsymbol{A}_3+\beta_2(\boldsymbol{A}_1\boldsymbol{A}_2+\boldsymbol{A}_2\boldsymbol{A}_1)+\beta_3(tr\boldsymbol{A}_1^2)\boldsymbol{A}_1, \tag{4}$$

where "tr" stands for the trace of the matrix, μ refers to the viscosity, α_1, α_2, β_1, β_2, β_3 represent the material constants (cf. [47]) of the working fluid. The expression of $\boldsymbol{A}_1$, $\boldsymbol{A}_2$, $\boldsymbol{A}_3$ are as follows:

$$\boldsymbol{A}_1=\nabla\boldsymbol{u}^*+(\nabla\boldsymbol{u}^*)^T\quad\text{and}\quad\boldsymbol{A}_n=\boldsymbol{u}^*\cdot\nabla A_n+\boldsymbol{A}_{n-1}\cdot\nabla\boldsymbol{u}^*+(\boldsymbol{A}_{n-1}\cdot\nabla\boldsymbol{u}^*)^T;\quad n=2,3. \tag{5}$$

2.3 Charge distribution

A thin layer of electrical charges called an electrical double layer (EDL) is formed, when a ionized solution comes into contact with the walls of the microchannel. This layer is the combination of two layers, namely the stern layer and the

diffuse layer. The stern layer is formed in the immediate vicinity of the channel walls. This layer consists of oppositely charged ions having a dimension of one atomic diameter. In the diffuse layer, which is formed next to the stern layer, counter ions migrate freely and a rapid thermal motion is set up. A zeta potential (ζ^*) is developed between these two layers, which maintains a constant value in the entire wall of the microchannel. Denoting the net charge density by ρ_e and fluid permitivity by ϵ, let us find the distribution of the electric potential Ψ^* by solving the Poisson-Boltzmann equation (cf. [48,49]) of the form

$$\nabla^2\Psi^* = -\frac{\rho_e}{\epsilon}\,. \tag{6}$$

In the present analysis, we assume that the length of the microchannel is much greater than the height of the microchannel, *i.e.*, $L \gg H$. Owing to this assumption, the electrical potential distribution is independent of the axial position. For an applied constant voltage gradient in ξ^*-direction in a $\varsigma:\varsigma$ symmetric electrolyte, the total ionic charge density may be expressed as $\rho_e = e\varsigma(n^+ - n^-)$, where e denotes the charge of a electron, ς stands for the ionic valency and $n^\pm$ denotes the densities of the positive/negative ions within the electrical double layer (EDL). For the present study, we may consider

$$n^\pm = \frac{n_0\exp(\mp e\varsigma\Psi^*/k_BT_a)}{1+2\wp\left\{\cosh(e\varsigma\Psi^*/k_BT_a)-1\right\}}\,, \tag{7}$$

in which n_0 is the ionic concentration, k_B the Boltzmann constant, T_a is the absolute temperature of the fluid at any location and $\wp$ stands for the steric factor (cf. [50]). Then from eq. (6), we have

$$\frac{\mathrm{d}^2\Psi^*}{\mathrm{d}\eta^{*2}} = \frac{2n_0e\varsigma}{\epsilon}\,\frac{\sinh(e\varsigma\Psi^*/k_BT_a)}{1+4\wp\,\sinh^2(e\varsigma\Psi^*/2k_BT_a)}\,. \tag{8}$$

The general solution for the electric potential Ψ^* can be obtained by solving the second-order differential equation (8) subject to appropriate conditions at the wall and the axis of the microchannel, given by

$$\left.\frac{\mathrm{d}\Psi^*}{\mathrm{d}\eta^*}\right|_{\eta^*=0} = 0, \qquad \Psi^*\big|_{\eta^*=H} = \zeta^*. \tag{9}$$

Introducing the dimensionless variables

$$\Psi = \frac{e\varsigma}{k_BT_a}\Psi^*, \qquad \zeta = \frac{e\varsigma}{k_BT_a}\zeta^* \quad \text{and} \quad \eta = \frac{\eta^*}{H}\,, \tag{10}$$

eq. (7) reads

$$\frac{\mathrm{d}^2\Psi}{\mathrm{d}\eta^2} = \frac{\kappa^2\sinh(\Psi)}{1+4\wp\sinh^2(\Psi/2)}\,, \tag{11}$$

where $\kappa = H/\lambda_D$ is the non-dimensional electro-osmotic parameter with $\lambda_D = \sqrt{\epsilon K_BT_a/2n_0e^2\varsigma^2}$ as the Debye length. In terms of the aforesaid non-dimensional variables the above boundary conditions (8) reduce to

$$\left.\frac{\mathrm{d}\Psi}{\mathrm{d}\eta}\right|_{\eta=0} = 0, \qquad \Psi\big|_{\eta=1} = \zeta. \tag{12}$$

For lower values of zeta potential ($|\zeta^*| \ll |k_BT_a/e\varsigma|$), one can ignore the steric effect ($\wp = 0$) and apply the Debye-Hückle approximation ($\sinh(e\varsigma\Psi^*/k_BT_a) \approx (e\varsigma\Psi^*/k_BT_a)$). But in order to make the present study more general, we do not apply any such approximation and for solving eq. (11) subject to the boundary conditions (12), we shall develop in the sequel, a suitable numerical scheme.

2.4 Velocity distribution

The governing equations (1) and (2) that describe the two-dimensional flow of an electrically conducting incompressible third-order fluid may be written in terms of Cartesian coordinates as

$$\frac{\partial u^*}{\partial\xi^*} + \frac{\partial\upsilon^*}{\partial\eta^*} = 0 \tag{13}$$

$$\begin{aligned}\rho\left(u^*\frac{\partial u^*}{\partial\xi^*} + \upsilon^*\frac{\partial u^*}{\partial\eta^*}\right) &= \mu\frac{\partial^2u^*}{\partial\eta^{*2}} + \alpha_1\left(u^*\frac{\partial^3u^*}{\partial\xi^*\partial\eta^{*2}} + \frac{\partial u^*}{\partial\xi^*}\frac{\partial^2u^*}{\partial\eta^{*2}} + \upsilon^*\frac{\partial^3u^*}{\partial\eta^{*3}} - 3\frac{\partial u^*}{\partial\eta^*}\frac{\partial^2\upsilon^*}{\partial\eta^{*2}}\right)\\ &\quad + 2\alpha_2\frac{\partial u^*}{\partial\eta^*}\frac{\partial^2u^*}{\partial\xi^*\partial\eta^*} + 6(\beta_2+\beta_3)\left(\frac{\partial u^*}{\partial\eta^*}\right)^2\frac{\partial^2u^*}{\partial\eta^{*2}} - \sigma B_0^2u^* + \frac{\rho_e\xi^*E_{\xi^*}}{L},\end{aligned} \tag{14}$$

while the boundary conditions read

$$\left.\frac{\partial u^*}{\partial \eta^*}\right|_{\eta^*=0}=0, \qquad \upsilon^*\big|_{\eta^*=0}=0, \qquad u^*+\beta^*\left.\frac{\partial u^*}{\partial \eta^*}\right|_{\eta^*=H}=0, \qquad \upsilon^*\big|_{\eta^*=H}=0. \tag{15}$$

Here α_1, α_2, β_2, β_3 represent the material moduli of the third-order fluid, μ is viscosity of the fluid, ρ the density of blood, σ the electrical conductivity, B_0 the applied magnetic field and β^* denote the length of velocity slip.

To obtain the solution eq. (14) subject to the boundary conditions (15), let us first introduce the dimensionless stream function

$$\overline{\psi}(\xi,\eta)=U_{HS}H\xi f(\eta) \quad \text{and} \quad \xi=\xi^*/H. \tag{16}$$

Now velocity components can be written as

$$u^*=\frac{\partial\overline{\psi}}{\partial\eta^*}=U_{HS}\xi f'(\eta) \quad \text{and} \quad \upsilon^*=-\frac{\partial\overline{\psi}}{\partial\xi^*}=U_{HS}f(\eta), \tag{17}$$

in which $U_{HS}=-\frac{\epsilon k_B T_a E_{\xi^*}}{\mu\varsigma e}$ stand for Helmholtz-Smoluchowski velocity. Equation (13) is automatically satisfied by the above expressions of u^* and υ^*, while eq. (14) assumes the following form:

$$f'''+Re(ff''-f'^2)+\epsilon_1(2f'f'''-ff^{iv})-(3\epsilon_1+2\epsilon_2)f''^2+6\phi f''^2f'''-Ha^2f'+\lambda\Psi''=0. \tag{18}$$

Moreover, the boundary conditions (15) take the forms

$$f''(\eta)\big|_{\eta=0}=0, \qquad f(\eta)\big|_{\eta=0}=0, \qquad f'(\eta)+\beta f''(\eta)\big|_{\eta=1}=0, \qquad f(\eta)\big|_{\eta=1}=0. \tag{19}$$

In the above-written equations, Re $(=\frac{U_{HS}}{\nu H})$ stands for the Reynolds number, ϵ_1 $\left(=\frac{\alpha_1 U_{HS}}{\mu H}\right)$, ϵ_2 $\left(=\frac{\alpha_2 U_{HS}}{\mu H}\right)$ and ϕ $\left(=\frac{(\beta_2+\beta_3)U_{HS}^2\xi^2}{\mu H^2}\right)$ are non-dimensional material parameters, Ha $(=\sqrt{\frac{\sigma}{\mu}}B_0H)$ is the Hartmann number, λ $\left(=\frac{H}{L}\right)$ denotes the aspect ratio and β $\left(=\frac{\beta^*}{H}\right)$ the non-dimensional velocity-slip parameter.

2.4.1 Perturbation analysis

Considering the parameter ϵ_1 to be small, we write

$$f(\eta)=f_0(\eta)+\epsilon_1 f_1(\eta)+\epsilon_1^2 f_2(\eta)+\cdots. \tag{20}$$

Substituting (20) in eq. (18), then equating the coefficients of like powers of ϵ_1 and ignoring the quadratic and higher power of ϵ_1, we have

$$f_0'''+Re\left(f_0f_0''-f_0'^2\right)-2\epsilon_2 f_0''^2+6\phi f_0''^2f_0'''-Ha^2f_0'+\lambda\Psi''=0, \tag{21}$$

$$f_1'''+Re\left(f_0''f_1+f_0f_1''-2f_0'f_1'\right)-4\epsilon_2 f_0''f_1''+6\phi\left(2f_1''f_0''f_0'''+f_0''^2f_1'''\right)-Ha^2f_1'=3f_0''^2-2f_0'f_0'''+f_0f_0^{iv}. \tag{22}$$

In a similar manner, the boundary conditions (19) can be rewritten in terms of f_0 and f_1 as

$$\begin{aligned} &f_0''(\eta)\big|_{\eta=0}=0, \quad f_0(\eta)\big|_{\eta=0}=0, \quad f_0'(\eta)+\beta f_0''(\eta)\big|_{\eta=1}=0, \quad f_0(\eta)\big|_{\eta=1}=0,\\ &f_1''(\eta)\big|_{\eta=0}=0, \quad f_1(\eta)\big|_{\eta=0}=0, \quad f_1'(\eta)+\beta f_1''(\eta)\big|_{\eta=1}=0, \quad f_1(\eta)\big|_{\eta=1}=0. \end{aligned} \tag{23}$$

2.5 Temperature distribution

In order to account for the heat transfer phenomenon, we consider the energy equation

$$\rho c_p(\boldsymbol{u}^*\cdot\nabla T^*)=-\boldsymbol{\nabla}\cdot\boldsymbol{q}+\sigma(\mathbf{E}\cdot\mathbf{E})+\frac{\mathbf{J}\cdot\mathbf{J}}{\sigma}+\boldsymbol{\Phi}, \tag{24}$$

in which c_p is the specific heat; the second and third terms on the right-hand side of eq. (24), respectively, represent the effects due to Joule heating and magnetic field, while Φ denotes the viscous dissipation term (cf. [51]) given by

$$\Phi=\mu\left(\frac{\partial u^*}{\partial\eta^*}\right)^2+\alpha_1\left(u^*\frac{\partial u^*}{\partial\eta^*}\frac{\partial^2u^*}{\partial\xi^*\partial\eta^*}+\upsilon^*\frac{\partial u^*}{\partial\eta^*}\frac{\partial^2u^*}{\partial\eta^{*2}}\right)+2(\beta_2+\beta_3)\left(\frac{\partial u^*}{\partial\eta^*}\right)^4. \tag{25}$$

In eq. (24), $\boldsymbol{q}$ denotes the heat flux based on the Cattaneo-Christov theory (cf. [42]), which satisfies the equation

$$\boldsymbol{q} + \lambda^* \left[\boldsymbol{u}^* \cdot \nabla \boldsymbol{q} - \boldsymbol{q} \cdot \nabla \boldsymbol{u}^* + (\nabla \cdot \boldsymbol{u}^*)\boldsymbol{q}\right] = -k\nabla T^*, \tag{26}$$

where λ^* denotes the thermal relaxation time, $\boldsymbol{u}^*$ the velocity vector and k the thermal conductivity of the fluid. It may be noted that for $\lambda^* = 0$ eq. (26) reduces to the classical Fourier's law of heat conduction. However, for the incompressible fluid considered here, eq. (26) takes the form

$$\boldsymbol{q} + \lambda^* \left[\boldsymbol{u}^* \cdot \nabla \boldsymbol{q} - \boldsymbol{q} \cdot \nabla \boldsymbol{u}^*\right] = -k\nabla T^*. \tag{27}$$

In general, the presence of thermal relaxation time in heat flux gives rise to a hyperbolic equation. The advantage of considering this equation is that we can study the heat transfer characteristics through waves. It will be clear in the sequel that with rise in thermal relaxation time, there is a breakdown of the fluid. Such types of properties make the Cattaneo-Christov heat flux from the classical Fourier's law of heat conduction.

From (24) and (27), we obtain

$$\begin{aligned}
&\rho c_p \left[u^* \frac{\partial T^*}{\partial \xi^*} + \upsilon^* \frac{\partial T^*}{\partial \eta^*} + \lambda^* \left(u^* \frac{\partial u^*}{\partial \xi^*} \frac{\partial T^*}{\partial \xi^*} + \upsilon^* \frac{\partial \upsilon^*}{\partial \eta^*} \frac{\partial T^*}{\partial \eta^*} + u^* \frac{\partial \upsilon^*}{\partial \xi^*} \frac{\partial T^*}{\partial \eta^*} + \upsilon^* \frac{\partial u^*}{\partial \eta^*} \frac{\partial T^*}{\partial \xi^*} + \upsilon^* \frac{\partial u^*}{\partial \eta^*} \frac{\partial T^*}{\partial \xi^*}\right.\right. \\
&\left.\left. + \; 2u^*\upsilon^* \frac{\partial^2 T^*}{\partial \xi^* \partial \eta^*} + u^{*2} \frac{\partial^2 T^*}{\partial \xi^{*2}} + \upsilon^{*2} \frac{\partial^2 T^*}{\partial \eta^{*2}}\right)\right] = k \frac{\partial^2 T^*}{\partial \eta^{*2}} + \sigma E_\xi^2 + \sigma B_0^2 u^{*2} + \mu \left(\frac{\partial u^*}{\partial \eta^*}\right)^2 \\
&+ \alpha_1 \left(u^* \frac{\partial u^*}{\partial \eta^*} \frac{\partial^2 u^*}{\partial \xi^* \partial \eta^*} + \upsilon^* \frac{\partial u^*}{\partial \eta^*} \frac{\partial^2 u^*}{\partial \eta^{*2}}\right) + 2(\beta_2 + \beta_3) \left(\frac{\partial u^*}{\partial \eta^*}\right)^4.
\end{aligned} \tag{28}$$

The thermal boundary conditions are

$$\left.\frac{\partial T^*}{\partial \eta^*}\right|_{\eta^*=0} = 0, \qquad T^* + k^* \left.\frac{\partial T^*}{\partial \eta^*}\right|_{\eta^*=H} = 0, \tag{29}$$

where k^* denotes the thermal-slip. Let T_w denote the wall temperature. We now introduce another dimensionless temperature variable

$$\Theta(\xi, \eta) = \frac{T^*}{T_w}. \tag{30}$$

In terms of this variable, eq. (28) reads,

$$(1 - \gamma\, Re\, Pr\, f^2)\Theta'' + Re\, Pr\, f(1 - \gamma\, f')\Theta' + S_p + Ha^2 Br f'^2 + Br f''^2 + \epsilon_1 Br \left(f' f''^2 - f'' f'''\right) + 2\phi Br f''^4 = 0, \tag{31}$$

in which $\gamma \left(= \frac{\lambda^* U_{HS}}{H}\right)$ is the dimensionless thermal relaxation parameter, $Pr \left(= \frac{\mu c_p}{k}\right)$ denotes the Prandtl number, $S_p \left(= \frac{\sigma E_\xi^2 H^2}{k T_w}\right)$ corresponds to the non-dimensional Joule heating parameter and $Br \left(= \frac{\mu \xi^2 U_{HS}^2}{k T_w}\right)$ is the Brinkman number.

Non-dimensional forms of the thermal boundary conditions are as follows:

$$\Theta'(\eta)\big|_{\eta=0} = 0, \qquad \Theta(\eta) + S_t \Theta'(\eta)\big|_{\eta=1} = 1, \tag{32}$$

$S_t \; (= \frac{k^*}{H})$ being the non-dimensional thermal slip.

2.6 Physical quantities

Here we emphasize upon mainly two important physical quantities, *viz.* i) skin friction and ii) Nusselt number. All these are calculated by using the following formulae by employing appropriate numerical scheme.

The non-dimensional forms of the local skin friction coefficient C_f^* and local Nusselt number Nu_{ξ^*} are, respectively, given by

$$C_f^* = \frac{2\tau_w}{\rho U_{HS}^2} \quad \text{and} \quad Nu_{\xi^*} = \frac{\xi^* q_w}{k T_w}, \tag{33}$$

where τ_w and q_w denote the wall shear stress and wall heat flux, respectively, given by

$$\begin{aligned}
\tau_w &= \mu \left.\frac{\partial u^*}{\partial \eta^*}\right|_{\eta^*=H} + \alpha_1 \left(u^* \frac{\partial^2 u^*}{\partial \xi^*} + \upsilon^* \frac{\partial^2 u^*}{\partial \eta^{*2}} + 2 \frac{\partial u^*}{\partial \xi^*} \frac{\partial u^*}{\partial \eta^*}\right)\Bigg|_{\eta^*=H} + 2 \frac{(\beta_2 + \beta_3)}{\rho} \left(\frac{\partial u^*}{\partial \eta^*}\right)^3 \Bigg|_{\eta^*=H} \\
q_w &= -k \left.\frac{\partial T^*}{\partial \eta^*}\right|_{\eta^*=H}.
\end{aligned} \tag{34}$$

Using (34) and the non-dimensional variables introduced earlier, we now have from (33)

$$C_f^* Re_\xi = f''(\eta) + \epsilon_1 \left[3f'(\eta)f''(\eta) - f(\eta)f'''(\eta)\right] + 2\phi \left(f''(\eta)\right)^3 \big|_{\eta=1} \quad \text{and} \quad Nu_\xi = -\xi\, \Theta'(\eta)\big|_{\eta=1}, \tag{35}$$

Re_ξ being the local Reynolds number.

3 Procedure for solving the non-linear equations numerically

Since the governing equations are highly non-linear, we have developed a suitable numerical procedure in order to solve them. The numerical scheme consists of the use of Newton's linearisation technique, the use of finite difference and the method of iteration. The method that we have used bears the advantage of quadratic convergence.

Let us substitute $f_0' = F_0$, $f_0'' = F_0'$, $f_0''' = F_0''$ and $f_1' = F_1$, $f_1'' = F_1'$, $f_1''' = F_1''$ in eqs. (21)-(22), so that the equations read

$$F_0'' + Re\left(f_0 F_0' - F_0^2\right) - 2\epsilon_2 F_0'^2 + 6\phi F_0'^2 F_0'' - Ha^2 F_0 + \lambda \Psi'' = 0, \tag{36}$$

$$F_1'' + Re\left(F_0' f_1 + f_0 F_1' - 2f_0' F_1\right) - 4\epsilon_2 F_0' F_1' + 6\phi\left(2F_1' F_0' F_0'' + F_0'^2 F_1''\right) - Ha^2 F_1 = 3F_0'^2 - 2f_0' F_0'' + f_0 F_0'''. \tag{37}$$

Also, the associated boundary conditions (23) take the following form:

$$\begin{aligned} F_0'(\eta)\big|_{\eta=0} &= 0, \qquad F_0(\eta) + \beta F_0'(\eta)\big|_{\eta=1} = 0, \\ F_1'(\eta)\big|_{\eta=0} &= 0, \qquad F_1(\eta) + \beta F_1'(\eta)\big|_{\eta=1} = 0. \end{aligned} \tag{38}$$

Following [52,53], the coupled non-linear system of differential equations (36), (37) has been solved numerically, by taking into consideration the boundary conditions (38). Adopting a similar procedure we have also solved the Poisson-Boltzmann equation (11) subject to (12) as well as the temperature equation (31) subject to the thermal boundary conditions (32).

Thus we have now the following set of differential equations:

$$\begin{aligned} A_1^i \left(\Psi''\right)^{i+1} + A_2^i \left(\Psi'\right)^{i+1} + A_3^i \left(\Psi\right)^{i+1} &= A_4^i, \\ B_1^i \left(F_0''\right)^{i+1} + B_2^i \left(F_0'\right)^{i+1} + B_3^i \left(F_0\right)^{i+1} &= B_4^i, \\ C_1^i \left(F_1''\right)^{i+1} + C_2^i \left(F_1'\right)^{i+1} + C_3^i \left(F_1\right)^{i+1} &= C_4^i, \\ D_1^i \left(\Theta''\right)^{i+1} + D_2^i \left(\Theta'\right)^{i+1} + D_3^i \left(\Theta\right)^{i+1} &= D_4^i, \end{aligned} \tag{39}$$

subject to the boundary conditions listed below,

$$\begin{aligned} \left(\Psi'(\eta)\right)^{i+1}\big|_{\eta=0} &= 0, \qquad \left(\Psi(\eta)\right)^{i+1}\big|_{\eta=1} = \zeta, \\ \left(F_0'(\eta)\right)^{i+1}\big|_{\eta=0} &= 0, \qquad \left(F_0(\eta)\right)^{i+1} + \beta\left(F_0'(\eta)\right)^{i+1}\big|_{\eta=1} = 0, \\ \left(F_1'(\eta)\right)^{i+1}\big|_{\eta=0} &= 0, \qquad \left(F_1(\eta)\right)^{i+1} + \beta\left(F_1'(\eta)\right)^{i+1}\big|_{\eta=1} = 0, \\ \left(\Theta'(\eta)\right)^{i+1}\big|_{\eta=0} &= 0, \qquad \left(\Theta(\eta)\right)^{i+1} + S_t\left(\Theta'(\eta)\right)^{i+1}\big|_{\eta=1} = 1. \end{aligned} \tag{40}$$

The quantities with superscript $(i+1)$ are calculated by using the values of the quantities with superscript i, whose values are already determined. In the system of eq. (39),

$$A_1^i = 1, \qquad A_2^i = 0, \qquad A_3^i = -\frac{\kappa^2 \sinh(\Psi^i)}{1 + 4\wp \sinh^2(\Psi^i/2)}, \qquad A_4^i = 0,$$

$$B_1^i = 1 + 6\phi F_0'^2, \qquad B_2^i = Re f_0 - 2\epsilon_2 F_0', \qquad B_3^i = -(Re f_0 + Ha^2), \qquad B_4^i = Re F_0^2 - \lambda\Psi'' + (2\epsilon_2 - 6\phi F_0'')F_0'^2,$$

$$C_1^i = A_1^i, \qquad C_2^i = Re f_0 - 4\epsilon_2 F_0' + 12\phi F_0' F_0'', \qquad C_3^i = -(2Re f_0' + Ha^2), \qquad C_4^i = 3f_0'^2 - 2f_0' F_0'' + f_0 F_0''',$$

$$D_1^i = 1 - \gamma Re Pr (f_0 + \epsilon_1 f_1)^2, \qquad D_2^i = Re Pr (f_0 + \epsilon_1)(1 - \gamma(F_0 + \epsilon_1 F_1)), \qquad D_3^i = 0,$$

$$\begin{aligned} D_4^i = -\Big[& S_p + Ha^2 Br \left(F_0 + \epsilon_1 F_1\right)^2 + Br\left(F_0' + \epsilon_1 F_1'\right)^2 + \epsilon_1 Br\Big(\left(F_0 + \epsilon_1 F_1\right)\left(F_0' + \epsilon_1 F_1'\right)^2 \\ & - \left(F_0' + \epsilon_1 F_1'\right)\left(F_0'' + \epsilon_1 F_1''\right)\Big) + 2\phi Br \left(F_0' + \epsilon_1 F_1'\right)^4 \Big]. \end{aligned}$$

System (39) was discretised for η-derivatives, using second-order central finite differences while the boundary conditions are discretised using forward/backward differences. At every iteration step, the equations reduce to a system of linear algebraic equations in the form of a tri-diagonal block matrix. The block matrix equations have then been solved by using Thomas algorithm (cf. [54]). The iterative procedure was continued until the absolute error committed between two consecutive operations is less than 10^{-6}, *i.e.*,

$$\mathrm{Max}\left\{\left|(\Psi(\eta))^{i+1}-(\Psi(\eta))^{i}\right|,\left|(F_0(\eta))^{i+1}-(F_0(\eta))^{i}\right|,\left|(F_1(\eta))^{i+1}-(F_1(\eta))^{i}\right|,\left|(\Theta(\eta))^{i+1}-(\Theta(\eta))^{i}\right|\right\}\leq 10^{-6}. \quad (41)$$

4 Entropy generation analysis

In the previous section, we have discussed the method of obtaining the numerical solution for velocity and temperature. In this section, we discuss the method of calculating the entropy generation rate in terms of various parameters involved in the present analysis. The calculation of entropy generation consists of four variables, *viz.* heat transfer, Joule heating, magnetic field intensity and fluid friction. The local entropy generation for the present problem (cf. [43,45]) may be expressed in the form

$$S_{gen}=\frac{k}{T_w^2}\left(\frac{\partial T^*}{\partial \eta^*}\right)^2+\frac{\sigma E_{\xi^*}}{T_w}+\frac{\sigma B_0^2 u^{*2}}{T_w}+\frac{\Phi}{T_w}. \quad (42)$$

In terms of non-dimensional variables, entropy generation may be expressed in its dimensionless form as

$$N_s=S_{gen}/S_g=\Theta'^2+S_p+Ha^2 Br f'^2+Br f''^2+\epsilon_1 Br\left(f'f''^2-f''f'''\right)+2\phi Br f''^4, \quad (43)$$

where S_g $(=\frac{k_f}{H^2})$ represents the characteristic entropy generation. For the present investigation, the entropy generation takes place due to a combination of four different effects, *viz.* i) conduction effect (heat transfer irreversibility) (HTI), ii) Joule heating irreversibility (JHI), iii) magnetic field irreversibility (MFI) and iv) fluid friction irreversibility (FFI). The Bejan number [55] for the present problem may be written in the form of a ratio

$$Be=\frac{HTI}{HTI+JHI+MFI+FFI}. \quad (44)$$

For the present problem, the Bejan number can vary from 0 to 1. If $Be=0$ then the irreversibility is dominated by the combined irreversibility due to Joule heating, magnetic field and fluid friction, while $Be=1$ corresponds to the particular limit, when irreversibility is dominated by heat transfer only. The contribution of heat transfer to the entropy generation is equal to the joint contribution of Joule heating, magnetic field and fluid friction. In this case, $Be=1/2$.

5 Validation of results

In this section, with an aim to validate the present analysis, we have made a comparison between the results of the present study and those reported in [16], where a simple problem of electro-osmotic flow was investigated analytically in the absence of any external magnetic field. While the present study considers high zeta potential, the earlier study was carried out by using Debye-Hückel approximation and the fluid considered was a second-order viscoelastic fluid. Moreover, the electro-osmotic flow characteristics of a third-order fluid has been investigated here for the situation, where the channel is under the influence of an external magnetic field. Figure 2 gives the distribution of axial velocity for the present study. The corresponding plots for the limiting case of a second-order fluid on the basis of the present study, using the approximation $\sinh(\Psi)\approx\Psi$ (Debye-Hückel approximation) and $Ha=0$ (in the absence of any magnetic field) have also been presented in fig. 2, along with the corresponding results for the second-order fluid, reported in [16]. The two plots presented at the top of fig. 2 validate the present study. Comparing all the plots presented in fig. 2, one finds that both the third-order effects and the influence of the magnetic field on fluid velocity in the axial direction are quite prominent. We further find that as expected, an externally applied magnetic field $(Ha=4.0)$ retards the flow. Moreover, the third-order effects are also significant.

6 Results and discussion

The numerical results computed/presented here correspond to blood, because the values of the different parameters have been taken from the data used in previous literatures [13,16,35,36,53,54]. The computational results have been obtained by considering the values of different physical variables mentioned in table 1.

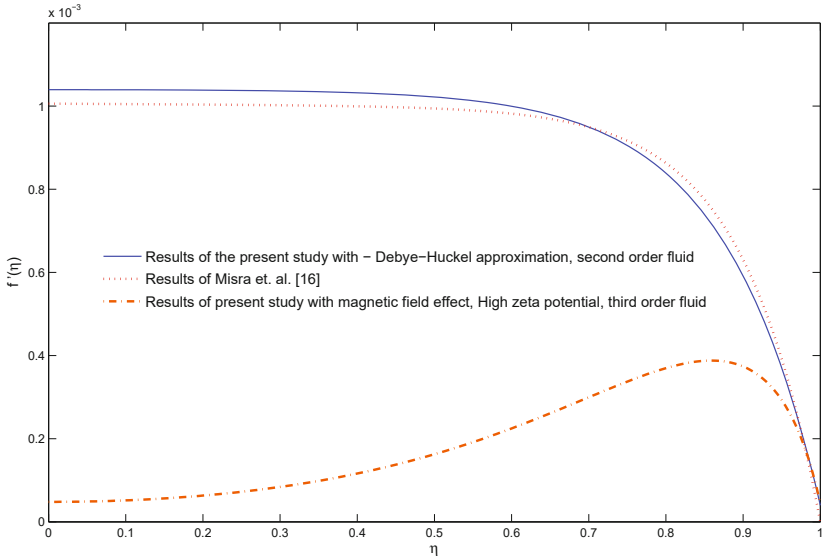

Fig. 2. Comparison of the results of the present study with those reported in [16], when $Re = 1.0$, $\kappa = 20.0$, $\epsilon_1 = 0.1$, $\lambda = 0.001$, $\wp = \beta = \epsilon_2 = \phi = Ha = 0.0$.

Table 1. Typical values of physical parameters.

Parameter	Symbol	Value	Unit
Half-channel height	H	10	μm
Charge of proton	e	1.6×10^{-19}	C
Electric field force in the axial direction	E_{ξ^*}	2×10^5	V/m
Viscosity of blood	μ_f	3.2×10^{-3}	Pa s
Density of blood	ρ	1050	kg m^{-3}
Electrical conductivity	σ	0.8	S/m
Thermal conductivity	k	0.58	W/(mK)
Boltzmann constant	k_B	1.38×10^{-23}	J/K
Debye length/EDL thickness	λ_D	3–35	nm
Channel length	L	0.005	m
Ionic concentration	n_0	1	mol/m^3
Average absolute temperature	T_a	300	K
Initial wall temperature	T_w	300	K
Ionic valency	ς	1	–
Steric factor	$\wp$	0.1–0.5	–
Electric potential of the walls	ζ^*	-0.25	V
Magnetic field strength	B_0	8–12	T (tesla)
Slip length	β^*/k^*	0–200	nm

It is assumed that the microchannel is under the influence of a strong magnetic field having strength 8–12 T (tesla). This range of magnetic field strength was considered in an experimental study (cf. [54]) on the orientation of erythrocytes in blood under the action of a strong magnetic field. If the parallel plates that represent the walls of the channel are taken to be made of silicon, a negative zeta potential will develop. In this case, the third order non-Newtonian fluid plays the role of a monovalent symmetric electrolyte. However, since the paper is motivated towards studying the electroosmotic flow in the realm of hemodynamics, the entire computational work has been performed by considering blood as the working fluid, as indicated above. We have taken $Re = 1$, $\lambda = 0.01$ and $\gamma = 0.1$, along with the following range of parametric values (estimated on the basis of the values provided in table 1):

$$0 \leq Ha \leq 8, \quad 0.0 \leq \beta \leq 0.2, \quad 5 \leq \kappa \leq 30, \quad 0 \leq \epsilon_1 \leq 0.2, \quad 0 \leq \epsilon_2 \leq 0.2,$$
$$0.5 \leq \zeta \leq 2, \quad 0 \leq S_t \leq 0.2, \quad 20 \leq Pr \leq 25, \quad -1.0 \leq S_p \leq 1.0, \quad 0 \leq Br \leq 0.1, \quad 0.1 \leq \phi \leq 0.7.$$

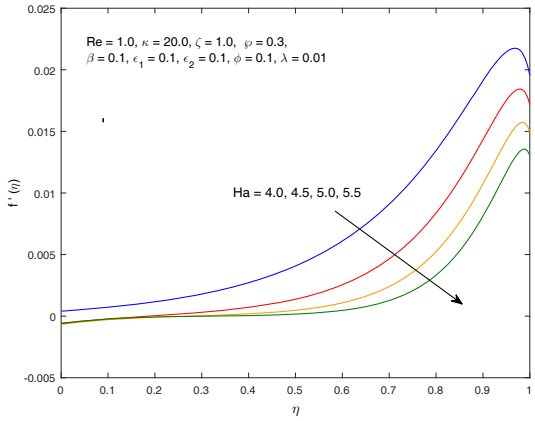

Fig. 3. Influence of magnetic field on velocity distribution.

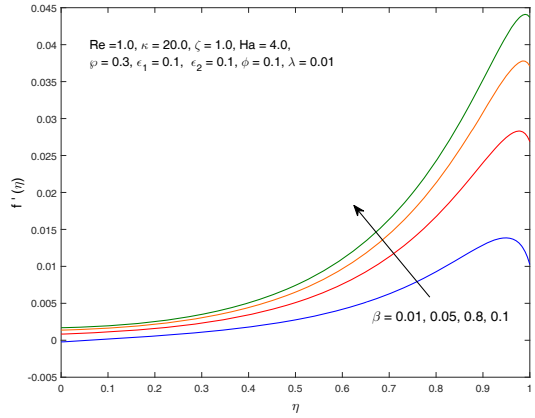

Fig. 4. Impact of velocity slip on velocity distribution.

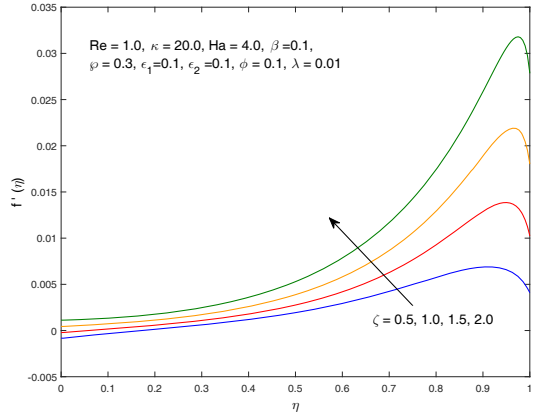

Fig. 5. Influence of surface zeta potential on velocity distribution.

Figures 3–8 illustrate the influence of different parameters on axial velocity. Figure 3 gives an idea of the changes in the distribution of velocity, as the magnetic field intensity is increased, while fig. 4 shows similar changes in the velocity, when velocity-slip increases. Similarly, changes taking place in the velocity distribution for changes in electroosmotic parameter (κ), material parameter (ϵ_1) of the third-order fluid (perturbation parameter), the surface zeta potential (ζ) and the steric factor ($\wp$) are depicted in figs. 5–8. It is known that high zeta potential that serves as a key factor of electrokinetic transport is developed in the fluid medium, when a strong electric current passes through the fluid. Figure 5 reveals that when the zeta potential (ζ) is high, the electroosmotic flow is enhanced. With an increase in the surface zeta potential, the non-dimensional electric potential in the interfacial double layer (DL) increases, whereby the boundary layer thickness also increases.

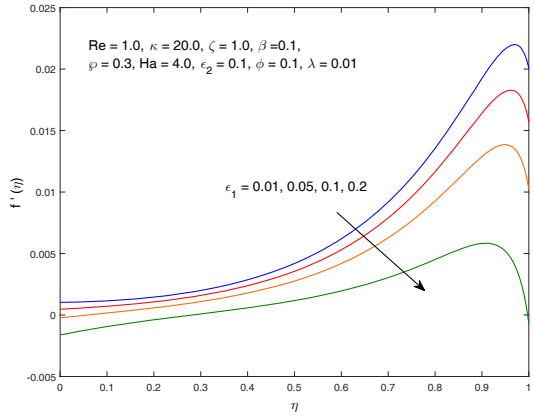

Fig. 6. Impact of ϵ_1 on axial velocity.

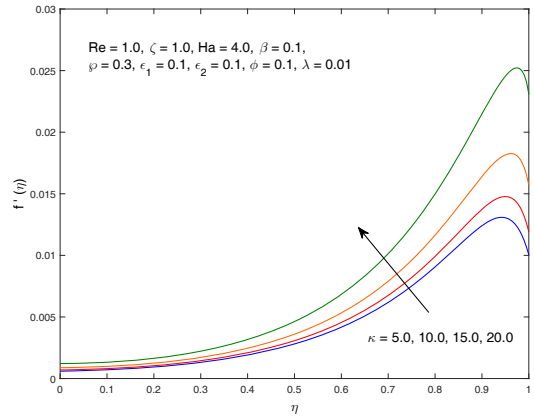

Fig. 7. Impact of electroosmotic parameter on axial velocity.

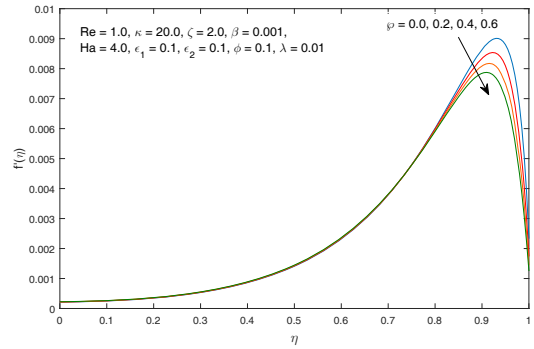

Fig. 8. Impact of steric factor on axial velocity.

Figure 6 shows that with an increase in the value of the material parameter ϵ_1, the velocity gradually reduces. This observation may be interpreted by saying that the viscoelastic effects become more prominent with a rise in the value of material parameter α_1 and thereby reduction of velocity takes place. Figure 7 reveals the effect of the phenomenon of electroosmosis. This figure shows that the velocity of the third-order fluid under consideration increases with a rise in the eletroosmotic parameter (κ) and that the velocity attains its minimum in the central region of the microchannel. The electroosmotic parameter (κ) being inversely proportional to the Debye length (λ_D), on the basis of the plots presented in fig. 7, we can make a conjecture that reduction of the electrical double layer (EDL) thickness leads to a significant rise in the electroosmotic velocity, which promotes the transport of mobile ions in the EDL formed in the vicinity of the wall of the microchannel. With a rise in the steric effect, there will be an amplification in the crowding of counterions within the EDL, owing to which the magnitude of the velocity reduces drastically in the vicinity of the capillary wall (cf. fig. 8).

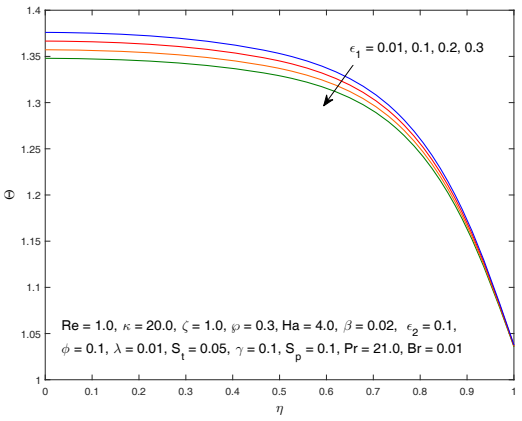

Fig. 9. Impact of ϵ_1 on temperature distribution.

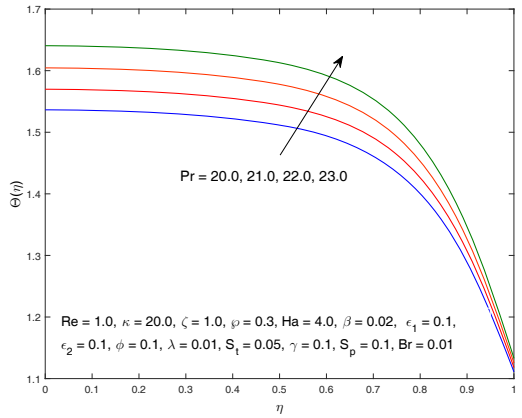

Fig. 10. Impact of Prandtl number on thermal distribution.

The effects of different physical parameters on the temperature distribution are shown in figs. 9–13. Figure 9 gives the impact of the third-order fluid parameter ϵ_1 on the distribution of fluid temperature. This figure shows that the temperature is maximum at the central line, while it is minimum at the capillary wall. One may observe from fig. 10 that the fluid temperature increases as the Prandtl number increases. Since specific heat capacity is directly proportional to the Prandtl number, it is apparent from fig. 10 that a fluid with high Prandtl number will have high heat capacity. As a consequence, it follows that if the Prandtl number is increased suddenly, the fluid temperature will be enhanced instantly. Owing to this, the thermal boundary layer thickness will be increased. It is apparent from fig. 11 that the fluid temperature is reduced when the magnetic field is increased. Figure 12 depicts the influence of thermal slip on the distribution of temperature. The different plots presented in this figure indicate that with an increase in thermal slip, the thermal boundary layer thickness increases. This may be attributed to the exchange of heat between the fluid and the microchannel walls. The heat exchange increases gradually with a rise in thermal slip, owing to which there is a rise in the thermal boundary layer thickness. From fig. 13, we can have a clear picture of the impact of Joule heating on the distribution of the fluid temperature. Here we consider both the case of heat generation (characterised by positive values of S_p) and heat absorption (characterised by negative values of S_p). This figure reveals that in both cases, the temperature of blood rises, when the value of the Joule heating parameter is raised.

Figure 14 gives the variation of the skin friction with the externally applied magnetic field strength. Different plots have been presented in the same figure, for varying values of ϕ, which is another parameter characterizing the nature of the third-order fluid. This figure shows that the magnitude of the skin friction reduces, when the value of Ha lies between 0 and 1.7, but for $Ha > 1.7$ the trend is completely reversed. This observation is common to all the values of ϕ investigated here and can be attributed to the generation of the Lorentz force that dominates the fluid viscosity. Figure 15 presents the variation of the Nusselt number as a function of the Hartmann number. This figure reveals that for $Ha \leq 2$, there occurs a rapid reduction in the heat transfer rate, but when $Ha > 2$, the heat transfer rate decreases very slowly. From the same figure, one can also observe that the heat generation effect due to Joule heating

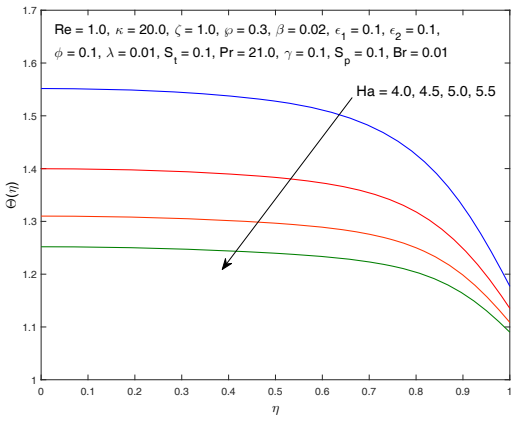

Fig. 11. Change in temperature distribution due to change in Hartmann number.

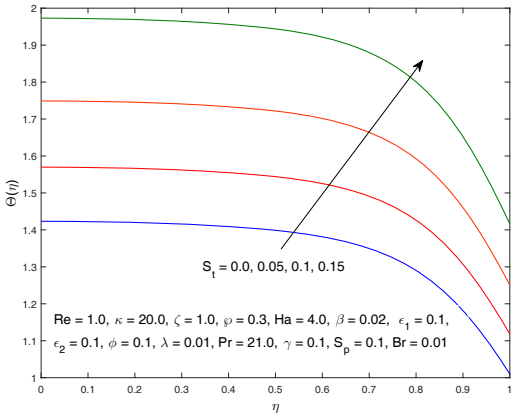

Fig. 12. Influence of thermal slip on temperature distribution.

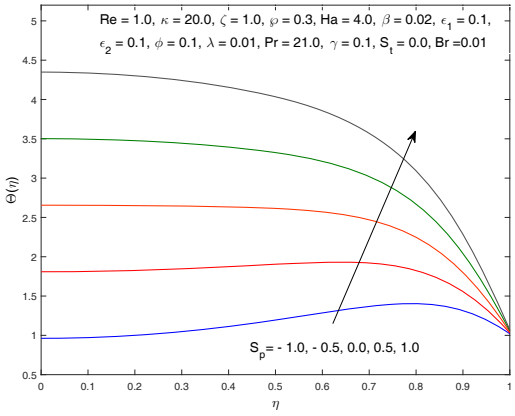

Fig. 13. Impact of Joule heating on temperature distribution (in the absence of thermal slip).

enhances the heat transfer rate on the capillary wall. Thus, both parameters S_p and Ha have major roles to play in controlling the heat transfer rate at the capillary wall. Figure 16 gives the variation of the Nusselt number with thermal relaxation parameter (γ), as the Prandtl number (Pr) changes between 20 and 23. This figure clarifies the mechanism of heat transfer in the vicinity of the wall. It may be noted that under the purview of the present study, the Nusselt number decreases, as the Prandtl number increases. All these observations can be justified by the fact that the Prandtl number varies directly with heat capacity of the fluid and that the kinetic energy due to the motion of the fluid particles increases significantly as the Prandtl number increases. From fig. 16, we further find that for all the values of Pr, the Nusselt number increases with increase in thermal relaxation. From the physical point of view, we may further

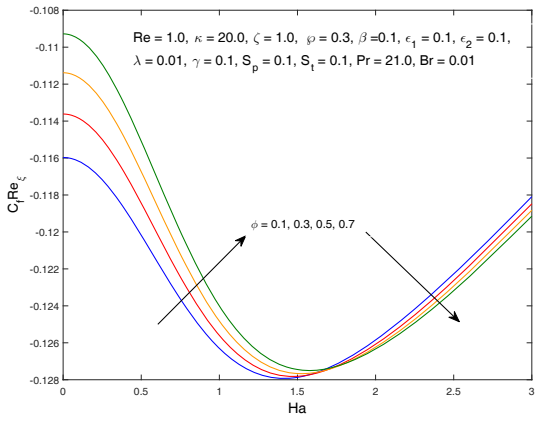

Fig. 14. Impact of Ha and ϕ on skin friction.

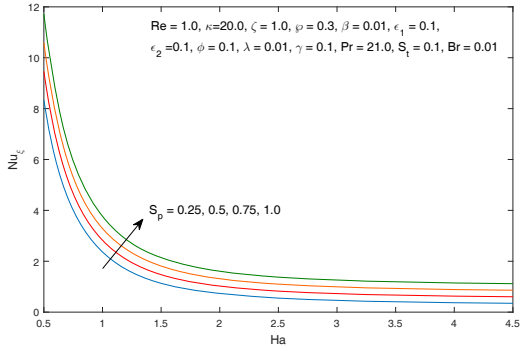

Fig. 15. Impact of Ha and S_p on Nusselt number.

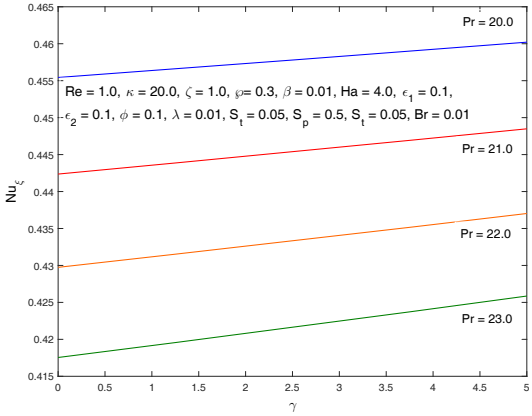

Fig. 16. Impact of Pr and γ on Nusselt number.

mention that where thermal relaxation increases, the time required for the transfer of heat from one particle to the neighbouring particle increases and this may be interpreted as the reason for the enhanced value of the Nusselt number.

Induction of entropy (N_s) during the fluid flow may take place due to thermal diffusion, Joule heating, magnetic field and viscosity. Thus in order to study the efficiency of fluid flow, it is necessary to analyse entropy generation. Figures 17 and 18 depict the impact of magnetic field (Hartmann number) and Joule heating on entropy generation. It is known that the fluid flow is hindered by the growing strength of the magnetic field, which reduces the shear flow and lowering of temperature. Entropy being directly to the temperature, it decreases with rise in the magnetic field strength (cf. fig. 17). Figure 18 reveals the impact of Joule heating on local entropy generation. It is observed that the total local entropy is enhanced as the quantum of Joule heating is increased. It may be further noted that while the change in entropy generation is very prominent in the vicinity of the capillary wall, it maintains a nearly constant value near the

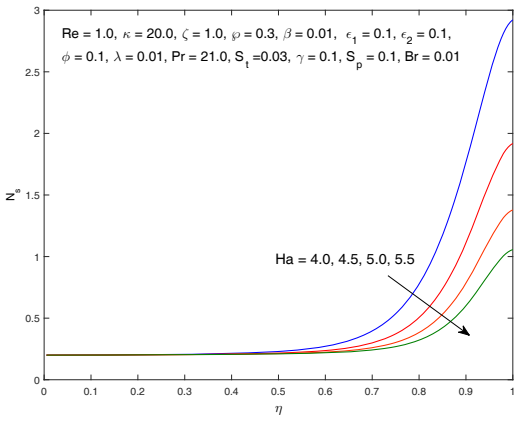

Fig. 17. Variation of entropy generation with change in Hartmann number.

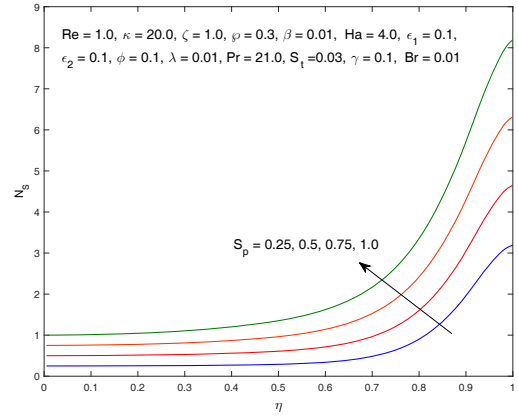

Fig. 18. Variation of entropy generation with change in Joule heating parameter.

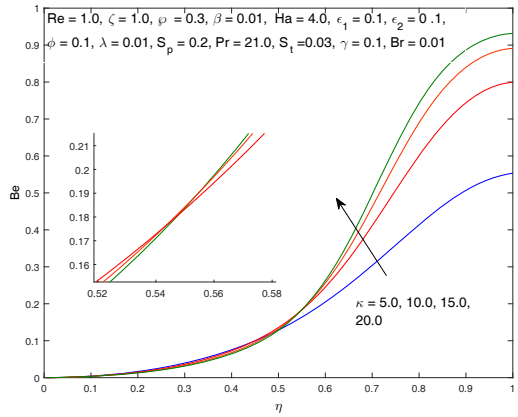

Fig. 19. Impact of electroosmosis on Bejan number.

axis. Figures 19 and 20 depict the variation of the Bejan number for different values of the electroosmotic parameter and thermal-slip parameter. It is noteworthy that the Bejan number is zero at the centre of the capillary. This leads us to make a conjecture that the entropy generation due to the combined impact of the fluid friction, the electric field and the magnetic field is not very relevant in the central region of the micro-vessels. From fig. 19, we also observe that thermal irreversibility changes significantly within the region of EDL for different values of the electroosmotic parameter. Moreover, it is seen that the Bejan number can alter the flow characteristics at $\eta = 0.55$. The impact of thermal-slip parameter on the Bejan number is illustrated in fig. 18. This figure shows that the Bejan number increases uniformly as the magnitude of thermal-slip increases. It is observed from fig. 21 that the thermal irreversibility decreases within the EDL as the Hartmann number increases, while a reverse trend is observed in the central region. It is worthwhile to

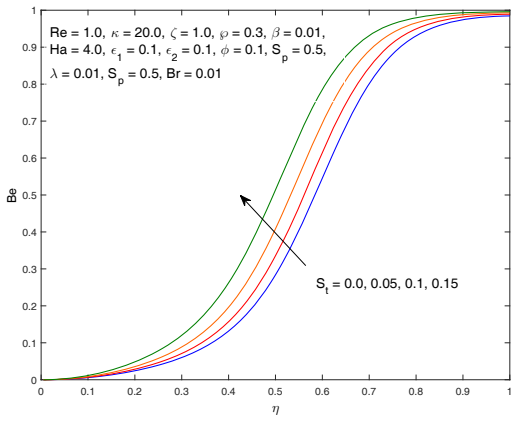

Fig. 20. Impact of thermal slip on Bejan number.

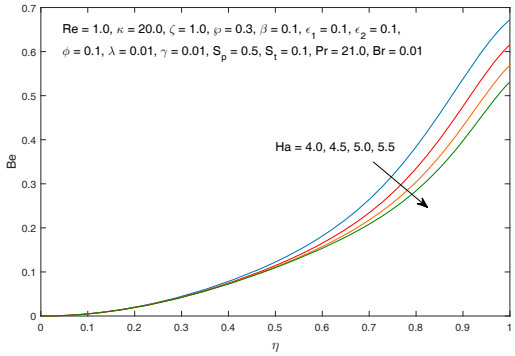

Fig. 21. Impact of Hartmann number on Bejan number.

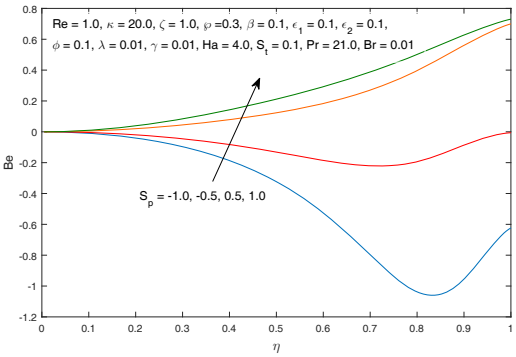

Fig. 22. Impact of Joule heating parameter on Bejan number.

further note here that the value of the Bejan number is highly dependent on the Joule heating parameter. Figure 22 gives a clear picture of the variation in the Bejan number during heat absorption. The observation from this figure implies that the heat transfer irreversibility is dominated by the combination of all other irreversibilities. One may observe a similar phenomenon happening at the boundary of the micro-vessels, when $S_p = -1/2$.

7 Concluding remarks

Using the concepts of cite dissociation models, a mathematical model has been developed here for studying the electro-magnetically driven flow of a third-order fluid. Heat transfer during the flow of the fluid has also been paid due attention by considering the Cattaneo-Christov heat flux. Major conclusions that can be drawn on the basis of the study are listed below.

– As the intensity of the applied magnetic field increases, the fluid velocity reduces, and for any magnetic field strength, the velocity attains its maximum near the wall.
– Fluid velocity increases with increase in the magnitudes of the velocity-slip, surface zeta potential, as well as the electroosmotic parameter.
– With an increase in the value of the material parameter ϵ_1 of the third-order fluid, both the fluid velocity and the temperature diminish.
– The steric factor counteracts with the transport mechanism to an appreciable extent.
– Heat transfer increases with increase in thermal slip and Joule hating, but it diminishes as the Hartmann number increases.
– The Nusselt number increases with increase in thermal relaxation, but it reduces with an increase in the Prandtl number.
– A steady increase in total entropy generation takes place in the vicinity of the walls of micro-vessels.
– The Bejan number increases with increase in both eletroosmotic parameter and thermal slip.

Finally on the basis of our study it can be concluded that the temperature for the Cattaneo-Christov heat flux model is less than that in Fourier's heat conduction. The temperature of the fluid gradually reduces, as thermal relaxation increases.

This work was supported by the Science and Engineering Research Board, Department of Science and Technology, Government of India, New Delhi through Grant No. SB/S4/MS: 864/14. The authors also wish to thank the reviewers for their comments and suggestion for the improvement of the earlier version of the manuscript.

Nomenclature

Symbol	Definition	Greek symbol	Definition
$\boldsymbol{u}^* = (u^*, v^*)$	Velocity vector	(ξ^*, η^*)	Cartesian coordinate of a point
$\boldsymbol{\tau}^*$	Stress tensor	ξ, η	Transformed variables
$\boldsymbol{f}_{\boldsymbol{B}}^*$	External body force vector	β^*	Velocity slip length
$\boldsymbol{E}$	Electric field vector	Ψ^*	Electric potential
$\boldsymbol{J}$	Electric current density	λ^*	Thermal relaxation time
$\boldsymbol{B}$	Magnetic field vector	σ	Electrical conductivity
$\boldsymbol{q}$	Heat flux	ς	Ionic valency
T^*	Temperature	ζ^*	Zeta potential at the wall
T_w	Wall temperature	λ_D	Debye Length
T_a	Absolute temperature	ζ	Non-dimensional zeta potential
$n^{\pm}$	Densities of positive and negative ion	$\overline{\psi}(\eta)$	Stream function
n_0	Ionic concentration	ρ_e	Total charge density
e	Protonic charge	α_1, α_2, β_1, β_2, β_3	Physical constants
L	Length of micro-channel	ϵ_1, ϵ_2, ϕ	Material parameters of the third order fluid
k_B	Boltzmann constant	λ	Aspect ratio
H	Height of the micro-channel	β	Velocity slip parameter
Re_ξ	Local Reynolds number	γ	Thermal relaxation parameter
U_{HS}	Helmholtz-Smoluchowski velocity	c_p	Specific heat
Re	Reynolds number	μ	Dynamic viscosity
Ha	Hartmann number	ρ	Density of fluid
τ_w	Wall shear stress	κ	Electro-osmotic parameter
k	Thermal conductivity		
k^*	Thermal slip		*Subscript*
Pr	Prandtl number		
S_p	Joule heating parameter	0	Terms associated with zeroth order
S_t	Thermal slip parameter	1	Terms associated with first order
q_w	Wall heat flux	w	Properties at the wall of micro-channel
C_f^*	Skin-friction		
Nu_{ξ^*}	Nusselt number		*Superscript*
S_{gen}	Entropy generation		
S_g	Characteristic entropy parameter	i	Iterative index
N_s	Non-dimensional entropy	$*$	Dimensional quantities
Be	Bejan number	$'$	Differentiation w.r.t. η

References

1. J. Lyklema, *Fundamentals of Interface and Colloid Science* (Academic Press, 2000).
2. H. Lowe, W. Ehrfeld, Electrochem. Acta **44**, 3679 (1997).
3. O. Worz, K.P. Jackel, T. Richter, A. Wold, Chem. Eng. Sci. **56**, 1029 (2001).
4. S.V. Gokhale, R.K. Tayal, V.K. Jayaraman, B.D. Kulkarni, Int. J. Chem. Reactor Eng. **3**, 1 (2005).
5. J. Koo, C. Kleinstreuer, Int. J. Heat Mass Transfer **47**, 3159 (2004).
6. J. Chen, M. Chu, K. Koulajian, X.Y. Wu, A. Giacca, Y. Sun, Biomed. Microdevices **11**, 1251 (2009).
7. D. Bhattaa, A.A. Michel, M. Marti Villalba, G.D. Emmerson, I.J.G. Sparrow, E.A. Perkins, M.B. McDonnell, R.W. Ely, G.A. Cartwright, Biosens. Bioelectron. **30**, 78 (2011).
8. D.R. Arifin, L.Y. Yeo, J.R. Friend, Biomicrofluidics **1**, 014103 (2007).
9. P. Abhimanyu, P. Kaushik, P.K. Mondal, S. Chakaraborty, Journal of Non-Newtonian Fluid Mechanics **231**, 56 (2016).
10. S. Chandra, J.C. Misra, J. Mol. Liq. **224(A)**, 818 (2016).
11. J.C. Misra, S. Chandra, H. Herwig, J. Hydrodyn. **27**, 350 (2015).
12. Z. Tan, J. Liu, Phys. Lett. A **381**, 2573 (2017).
13. J.C. Misra, S. Chandra, G.C. Shit, P.K. Kundu, Appl. Math. Mech. **35**, 749 (2014).
14. J.C. Misra, S. Chandra, Cent. Eur. J. Phys. **12**, 274 (2014).
15. J.C. Misra, S. Chandra, J. Hydrodyn. **25**, 309 (2013).
16. J.C. Misra, G.C. Shit, S. Chandra, P.K. Kundu, Appl. Math. Comput. **217**, 7932 (2011).
17. J.R. Kelner, M.S. Roos, P.R. Brakeman, T.F. Budinger, Magn. Reson. Med. **16**, 139 (1990).
18. E.E. Tzirtzilakis, Phys. Fluids **17**, 077103 (2005).
19. Y. Kinouchi, H. Yamaguchi, T.S. Tenforde, Bioelectromagnetics **17**, 21 (1996).
20. O. Aydin, A. Kaya, Appl. Math. Model. **33**, 4086 (2009).
21. A. Sinha, J.C. Misra, ASME J. Heat Transf. **136**, 112701 (2014).
22. A. Sinha, J.C. Misra, J. Mech. **30**, 491 (2014).
23. J.C. Misra, A. Sinha, Heat Mass Transf. **49**, 617 (2013).
24. J.C. Misra, A. Sinha, Spec. Top. Rev. Porous Media Int. J. **4**, 147 (2013).
25. J.C. Misra, S. Chandra, G.C. Shit, P.K. Kundu, J. Mech. Med. Biol. **13**, 1350013 (2013).
26. A. Sinha, J.C. Misra, Appl. Math. Mech. **33**, 649 (2012).
27. J.C. Misra, A. Sinha, G.C. Shit, J. Mech. Med. Biol. **11**, 547 (2011).
28. J.C. Misra, A. Sinha, G.C. Shit, Int. J. Biomath. **4**, 207 (2011).
29. J.C. Misra, G.C. Shit, S. Chandra, P.K. Kundu, J. Eng. Math. **59**, 91 (2011).
30. J.C. Misra, A. Sinha, G.C. Shit, Appl. Math. Mech. **31**, 1405 (2010).
31. J.C. Misra, G.C. Shit, J. Appl. Mech., Trans. ASME (USA) **76**, 06106 (2009).
32. J.C. Misra, G.C. Shit, Appl. Math. Comput. **210**, 350 (2009).
33. J.C. Misra, S. Maiti, G.C. Shit, J. Mech. Med. Biol. **8**, 507 (2008).
34. J.C. Misra, A. Sinha, J. Hydrodyn. **27**, 647 (2015).
35. J.C. Misra, S. Chandra, J. Hydrodyn. **25**, 309 (2013).
36. J.C. Misra, G.C. Shit, S. Chandra, P.K. Kundu, J. Eng. Math. **59**, 91 (2011).
37. J.C. Misra, B. Pal, A.S. Gupta, Math. Models Methods Appl. Sci. **8**, 1323 (1998).
38. T. Hayat, M. Imtiaz, A. Alsaedi, S. Almezal, J. Mag. Magn. Mater. **401**, 296 (2016).
39. M. Mustafa, AIP Adv. **5**, 047109 (2015).
40. S. Han, L. Zheng, C. Li, X. Zhang, Appl. Math. Lett. **38**, 87 (2014).
41. M. Ciarletta, B. Straughan, Mech. Res. Commun. **37**, 445 (2010).
42. A. Sarkar, P.K. Kundu, Eur. Phys. J. Plus **132**, 534 (2017).
43. F.A. Soomro, R.U. Haq, Z.H. Khan, Q. Zhang, Eur. Phys. J. Plus **132**, 412 (2017).
44. C. Sulochana, G.P. Ashwinkumber, N. Sandeep, Eur. Phys. J. Plus **132**, 387 (2017).
45. M.I. Afridi, M. Qasim, S. Shafie, Eur. Phys. J. Plus **132**, 404 (2017).
46. R.J. Moreau, *Magnetohydrodynamics* (Springer, 1990).
47. K. Ayun, M.Y. Khan, M. Asraf, J. Ahmad, Q. M-Ul-Hassan, Eur. Phys. J. Plus **132**, 552 (2017).
48. R.F. Probstein, *Physicochemical Hydrodynamics* (Wiley, New York, 1994).
49. R.J. Hunter, *Zeta Potential in Colloid Science: Principles and Applications* (Academic Press, London, 1981).
50. S. Sarkar, S. Ganguly, P. Dutta, Int. J. Heat Mass Transer **104**, 1325 (2017).
51. S.A. Shehzad, T. Hussain, T. Hayat, M. Ramzan, A. Alsaedi, J. Cent. South Univ. **22**, 360 (2015).
52. V. Lakshmikantham, A.S. Vatsala, *Generalized Quasilinearization for Nonlinear Problems (Mathematics and Its Applications)* (Kluwer Academic, Dordrecht, 1998).
53. J.C. Misra, A. Sinha, B. Mallick, Physica A **470**, 330 (2017).
54. L.H. Thomas, *Elliptic Problems in Linear Difference Equations over a Network*, Watson Sci. Comput. Lab. Rept. (Columbia University, New York, 1949).
55. A. Bejan, ASME J. Heat Transf. **101**, 718 (1979).